Influence of alloying elements (Cu, Ti, Nb) on the microstructure and corrosion behaviour of AlCrFeNi-based high entropy alloys exposed to oxygen-containing molten Pb

Hao Shi[a,*], Renate Fetzer[a], Adrian Jianu[a], Alfons Weisenburger[a], Annette Heinzel[a], Fabian Lang[a], Georg Müller[a]

[a] *Institute for Pulsed Power and Microwave Technology (IHM), Karlsruhe Institute of Technology (KIT), Hermann-von-Helmholtz-Platz 1, 76344 Eggenstein-Leopoldshafen, Germany*

* Corresponding author. E-mail address: hao.shi@kit.edu (H.Shi)

Keywords: High entropy alloy; Corrosion; High temperature; Microstructure; Molten Pb.

Abstract

Three high entropy alloys (HEAs), based on Al-Cr-Fe-Ni-X (X: Cu, Ti or Nb), have been designed and prepared. The sample with Cu addition has formed FCC solid solutions while the other two have formed FCC matrix plus inter-metallic phases (B2-Ni(Al,Ti) or Laves). The corrosion tests in oxygen-containing molten Pb at 600 °C indicate that Cu or Ti addition degrades the corrosion resistance of HEAs. Sample with Nb addition shows promising corrosion behaviour. Besides, all three alloys have experienced phase transformation after 1000 and 2000 h exposure. New phases like BCC, B2-NiAl, σ-phase, η-phase or-/and-Ni_3Nb have been identified after exposure.

1. Introduction

Heavy liquid metals (HLMs) like Pb or Pb-Bi eutectic (LBE) are proposed as potential heat transfer or storage media for advanced energy systems, namely Gen-IV lead-cooled fast reactors (Gen-IV LFRs), accelerator driven system (ADS), concentrated solar power (CSP), liquid metal batteries (electrode) [1-7]. However, using HLM at elevated temperature often results in compatibility issues with structural steels [3, 8-10]. For instance, ferritic steels (e.g. T91, HT9) are susceptible to the liquid metal embrittlement (LME) when in contact with liquid Pb/LBE at around 350 °C under loading condition [11-12]. Although austenitic steels are more resistant to LME, the severe corrosion attack at temperature above 500 °C challenges their applications [13-14]. The corrosion of steels in HLMs is mainly driven by the selective dissolution of alloying elements from the base materials, leading to dissolution-type or inter-granular attack [9-10, 13-14]. Moreover, high solubility of Ni (solubility in Pb: Ni>Cr>Fe [3]) in HLMs results in the ferritization of the austenitic structure [10, 13]. Therefore, the research work now are focused on designing advanced structural materials like alumina forming austenitic alloys (AFA), high entropy alloys (HEAs), and max-phase compound (MAX), which might mitigate the degradation/corrosion issues of structural materials exposed to HLMs at temperature above 550 °C [10, 15-17].

Among these advanced materials, HEAs, which break with the design strategy for traditional alloys/steels, have shown excellent properties [18-21]. Instead of one or two principle elements in conventional structural metals, the multi-principle elements concept has been applied in HEAs in order to obtain a material with "cocktail effect" (super properties can be obtained by mixing multiple elements

which could not be obtained from any one independent element) [22-23]. Within the various combinations, the widely investigated Al-Co-Cr-Fe-Ni system has shown excellent mechanical and corrosion properties [24-28]. However, considering the quite expensive price and irradiation sensitivity of cobalt (Co) in nuclear environment [29], Co-free Al-Cr-Fe-Ni HEA model alloys with FCC phase dominant alloy matrix have been designed [30]. The study of Al-Cr-Fe-Ni alloys show their promising corrosion resistance exposed to various conditions like molten Pb and steam [30-31]. However, the microstructure stability and mechanical properties need to be further improved for high temperature applications. This can be achieved by adding a fifth element, either for stabilizing the phase compositions [32-34] or for precipitation of strengthening phases like Fe_2Nb, B2/$L2_1$ phase [35-36].

Some research works have reported the influences of alloying elements (Cu, Ti, Nb) on the microstructure, corrosion and mechanical properties of HEAs alloys at different experimental conditions [31-59].

Gwalani et al. [32] have investigated the influence of Cu addition on the microstructure of $Al_{0.3}CrCuFeNi_2$. The analytical results indicate that Cu not only segregates at the inter-dendrites, but also help stabilizing the $L1_2$ (γ′) phase. Another investigation from Dabrowa et al. [37] has proved that the microstructure of $AlCoCrCu_xFeNi$ (x=0.5, 1) transforms from BCC to BCC plus FCC by increasing the Cu content. The oxide formed on all samples at 1000 °C is mainly α-Al_2O_3. Moreover, during the early stage of oxidation, the oxidation rate of candidate alloys decreases as the amount of Cu increases, which is also reported for the oxidation of Fe-17Ni-17Cr-7.7Al (at.%) austenitic alloys with different Cu contents (0 to 7 at.%) in air at 1000 °C [40]. The authors clarify that Cu addition reduces the oxygen solubility in bulk alloy. Unfortunately, samples with Cu addition show an oxide scale exfoliation, which is less visible on Cu-free AlCoCrFeNi alloy. Such phenomenon is also observed by other research groups, namely, spallation of α-Al_2O_3 scale formed on $Al_{23}Co_{15}Cr_{23}Cu_8Fe_{15}Ni_{15}$ and $Al_{17}Co_{17}Cr_{17}Cu_{17}Fe_{17}Ni_{17}$ when oxidized in air at 800 to 1000 °C [38], and oxide scale exfoliation in spite of the type of oxides formed on $Al_xCoCrCuFeNi$ (x=0, 0.5, 1, 1.5, 2) at 1000 °C in air [39].

Titanium has been added in various HEAs systems, such as Al-Co-Cr-Fe-Ni-Ti [41-48], Al-Cr-Fe-Ni-Ti [49-50], Al-Co-Cr-Cu-Fe-Ni-Ti [51-52], in order to obtain alloys with excellent mechanical or corrosion properties. The strengthening effect of Ti is mainly due to the solid solution strengthening and precipitation of γ' phase (e.g. $Ni_3(Al,Ti)$, Ni_3Al), Heusler ($L2_1$, e.g. Ni_2TiAl) or/and B2 phase [41, 42, 45]. For instance, Shun et al. [41] reported an increase in hardness of over 80% in $Al_{0.3}CoCrFeNiTi_{0.1}$ when compared with Ti-free samples. The corrosion/oxidation behaviour of Ti-containing HEA alloys was also investigated [31, 44, 46]. Chang et al. [44] investigated the oxidation of $Al_xCo_{1.5}CrFeNi_{1.5}Tiy$ (x+y=0.5) in air at 900 °C. The oxide layer formed on $Al_{0.2}Co_{1.5}CrFeNi_{1.5}Ti_{0.3}$ consists of an outermost Fe and Ti rich oxide layer, a continuous Cr_2O_3 middle layer and an internal Al oxidized layer. Erdogan et al. [46] has studied the oxidation behaviour of $CoCrFeNiAl_xTi_y$ (x = 0, 0.5, 1; y = 0, 0.5) in air at 1000 °C with different exposure times. By increasing the amount of Ti, the mass gain of the sample increases as well. The types of oxides formed during oxidation also change as the exposure time increases. As an example, $CoCrFeNiAl_{0.5}Ti_{0.5}$ has

formed Cr_2O_3 and Fe_2TiO_5 outer layer and thin inner alumina layer after 5 h exposure. Then, mixed oxides of spinel, alumina, Cr_2O_3, Fe_2TiO_5 and TiO_2 have been identified in the subsequent oxidation. Results from a previous study indicate that the thickness of the oxide scale formed on AlCrFeNiTi sub-system is around 23 times thicker than that of Ti-free alloys in steam at 1200 °C [31]. All of the results have indicated that adding Ti increases the mass gain during oxidation because of the formation of less protective TiO_2 oxide layer.

The segregation of Laves inter-metallic phase has been widely reported in varies HEA systems with Nb addition, namely AlCoCrFeNiNb [53], $CoCrFeNiNb_x$ (x: 0 to 0.75) [52-53], $(FeCoNiCuCr)_{100-x}Nb_x$ (x: 0 to 10 at.%) [56], Al-Co-Cr-Fe-Nb-Ni [57], 9Fe-6Al-6Nb-18Cr-31Ni [58]. Most of the studies are focused on the influence of Nb addition on the microstructure (e.g. in as produced and heat treated state) and mechanical properties of HEA alloys. Alloying with Nb addition usually improves the strength and hardness in expense of the ductility because of the brittle nature of Laves phase [54-58]. However, a balance of strength and ductility can be achieved by a combination of solid solution hardening and formation of secondary Laves phase [55]. In addition, the influence of thermal aging on the microstructure evaluation of Nb-containing HEA alloys have been reported as well [57-58]. Sub-micron NiAl, Laves and δ phase ($D0_a$ crystal structure) have been observed in the matrix of Fe-Al-Nb-Cr-Ni with variations of Fe, Al and Nb contents after thermal treatment at 800 to 1000 °C [58]. There is a competition between the sub-micron NiAl and δ phase precipitates depending on the ratio of Al and Nb. The influence of Nb on the corrosion/oxidation properties is rarely investigated [31, 59]. One study of oxidation behaviour of Al-Cr-Fe-Ni with Nb addition has shown the improved corrosion resistance of the alloy in steam environment at 1200 °C [31]. Another investigation of the electrochemical corrosion resistance of $CoCrFeNiNb_x$ (x: 0 to 0.75) has displayed the positive influence with increasing Nb concentration [59].

Considering the beneficial effects of Cu, Ti and Nb on the mechanical properties of HEAs, three HEAs with addition of 5 at.% Cu, Ti or Nb are designed and produced in the current study. Then their high temperature corrosion behaviour in oxygen-containing molten Pb as well as microstructure evolution during exposure is evaluated. The results presented in this paper will help understand the influences of Cu, Ti or Nb addition on the corrosion behaviour and microstructure stability of HEAs at high temperature and in corrosive environments.

2. Materials and methods

2.1 Alloy production

The as cast alloys are produced by an arc melting facility (MAM-1 Glovebox Version) produced by Edmund Bühler GmbH. Pure metal elements (purity > 99.99%) with the proposed chemical compositions are mixed and melted by a non-consumable tungsten electrode in a water chilled copper mold under argon atmosphere. The ingots are flipped over and re-melted at least five times in order to homogenize the compositions. Thermodynamic phase calculation has been performed by Thermo-calc software. The database used in this study is TCHEA4.

2.2 Corrosion tests

The corrosion test has been performed in a stagnant molten Pb corrosion facility with controlled oxygen concentration, called COSTA (**CO**rrosion test stand for **ST**agnant liquid **A**lloys) [10]. Before the corrosion test, solid Pb is melted and exposed to reducing oxygen condition for 3 days, followed by one week exposure to the selected oxygen content and temperatures. The oxygen concentration in liquid Pb is kept constantly with 10^{-6} wt.%. The samples used for the corrosion experiment are cut in pieces with a thickness of 1.2 mm and a diameter of 10 mm. A hole with a diameter of 1.5 mm is drilled in each sample, which is close to the edge in order to hang the sample during the corrosion test. Then the samples are grinded with 1200 grit surface finish, cleaned with ethanol and acetone, and dried. In order to prevent the sample from floating during the corrosion test, samples are hanged by a Mo-wire and fixed to the alumina holder. A dedicated glove-box conditioned to the similar oxygen partial pressure as in the furnace is used to introduce the samples. The samples are exposed to molten Pb at 600 °C, with 10^{-6} wt.% oxygen concentration in order to promote the formation of a protective oxide scale on the metal surfaces [10]. Two samples from each composition are tested, one is exposed for 1000 h and the other for 2000 h.

After the corrosion tests, the samples are extracted from molten Pb by using the same conditioned glove-box as for the loading process. Then, remaining Pb attached on the samples is cleaned by immersing the samples into a solution of ethanol, acetic acid and hydrogen peroxide (1:1:1) for 15 min, which is accepted as standard procedure for Pb cleaning [60].

2.3 Characterization

The Vickers hardness has been measured on all as cast alloys according to the ASTM E92 (Standard Test Method for Vickers Hardness of Metallic Materials). All the sample surfaces are grinded with 1200 and 2400 grit surface finish before the measurements. Then, the diamond indenter shaped in a right pyramid with a square base, with a loading of 100 P (Pond), is applied on the sample for a loading time of 10 s. The two diagonals of the identation left on sample surface (after remove the load) are measured by microscope. The average value is used for the hardness calculation according to the following equation (1). More than 10 points are measured on each sample and the average value is considered.

$$HV = \frac{1854.4 \cdot P}{d^2} \quad (1)$$

Where *HV* is Vicker hardness (kp/mm^2), *P* is the force applied to the diamond, and *d* is average value of diagonals of the identation (μm).

The phase compositions of all samples (before/after corrosion test) have been analyzed by X-ray diffraction (XRD, Seifert PAD II) with Cu Kα1 radiation (λ=0.15406 nm, 40 kV and 30 mA) in Bragg–Brentano geometry (θ-2θ) with a step size of 0.02° and a scan speed of 0.1 °/min.

The microstructures of the samples are characterized by Scanning Electron Microscopy (SEM, model: Zeiss LEO 1530 VP with a Field emission gun), equipped with an Energy Dispersive X-Ray Spectrometer

(EDX). A focused electron beam with energy varying from 10 to 20 keV and working distance of 10 mm is used in this characterization.

The sample surface (after corrosion test) is directly characterized by SEM/EDX without further preparation. In case of cross section analysis, an electroplated nickel layer with a thickness around 30 µm is deposited to protect the surface oxide scale from detachment during sample preparation. Then the samples are fixed and embedded with resin. All embedded samples are grinded by 1200 and 2400 grit sand paper, polished with diamond paste (1 µm diameter diamond particles), and sputtered with a thin, electrically conducting layer of gold.

3. Results

3.1 Alloy design

The quaternary HEA model alloy $Al_8Cr_{23}Ni_{35}Fe_{34}$ (at.%), called HEA-ref, which shows excellent corrosion resistance to oxygen-containing molten Pb [30], has been considered as a backbone composition for the alloy design. Three alloys with addition of a fifth principle element (Cu, Ti or Nb) have been designed. The concentration of the fifth element is fixed to a value around 5 at.%, which is the minimum value of an alloying element to be considered as a principle element in HEAs, as early defined by Yet et al. [18].

In addition, some empirical parameters proposed for HEA design [18, 23, 61, 62], namely enthalpy of mixing (ΔH_{mix}), atomic size difference (δr), Ω ($\Omega = (\Sigma ci T_{m,i})\Delta S_{mix} / |\Delta H_{mix}|$), and valence electron concentration (*VEC*), have been employed to further optimize the chemical compositions and predict the phase formation. The value of each parameter has been defined according to the literatures [18, 23, 61, 62], shown in Table 1, in order to search for the HEAs with FCC dominant alloy matrix (in as cast condition). Based on the required range of ΔH_{mix}, δr and Ω, only single FCC solid solution forms when *VEC* is larger than 7.8 while FCC plus inter-metallic compounds tend to form as *VEC* is between 7.5 and 7.8 [61-62].

Table 1
Required values of ΔH_{mix}, δr, Ω and *VEC* for HEA design.

Microstructure	ΔH_{mix} (KJ/mol)	δr (%)	Ω	*VEC*
FCC solid solution	$-15 < \Delta H_{mix} < 5$	$1 < \delta r < 6.6$	>1.1	>7.8
FCC+IM	$-15 < \Delta H_{mix} < 5$	$1 < \delta r < 6.6$	>1.1	$7.5 < VEC < 7.8$

Table 2 summarizes the nominal compositions of designed HEAs, and the calculated results of empirical parameters (ΔH_{mix}, δr, Ω and *VEC*) used to predict the phase compositions. Comparing the calculated values with the design rules in Table 1, HEA-Cu tends to form single FCC solid solution while HEA-Ti and HEA-Nb should form FCC plus IM in alloy matrix.

Table 2
Nominal compositions of HEAs (at.%), and calculated values of ΔH_{mix}, δr, Ω and *VEC*.

Code	Nominal composition (at.%)	ΔH_{mix}	δr	Ω	*VEC*	Predicted Phase
HEA-Cu	$Al_{8.0}Cr_{22.0}Fe_{32.0}Ni_{33.0}Cu_{5.0}$	-5.45	4.02	3.82	7.97	FCC
HEA-Ti	$Al_{7.9}Cr_{22.0}Fe_{31.9}Ni_{33.2}Ti_{5.0}$	-11.18	5.25	1.89	7.63	FCC+IM
HEA-Nb	$Al_{8.2}Cr_{21.4}Fe_{30.3}Ni_{35.0}Nb_{5.1}$	-10.92	4.97	1.98	7.71	FCC+IM

Moreover, thermo-dynamic calculation of each HEA is performed in order to predict the phase formed in as cast alloys. Fig. 1 shows the calculated phase compositions of each alloy as a function of temperature. The as cast alloys are expected to maintain the phases obtained directly from liquid state due to a relatively fast cooling rate. Therefore, only the phases obtained at the right side of the phase diagram are considered, which means the phase composition at the temperature above 1100 ˚C. According to the calculation result shown in Fig. 1 (a), only single FCC phase will form in HEA-Cu during solidification. In case of HEA-Ti, the phase composition after solidification includes FCC and BCC phases. Replacing the Ti with Nb, the alloy is predicted to form FCC and Laves from liquid metal.

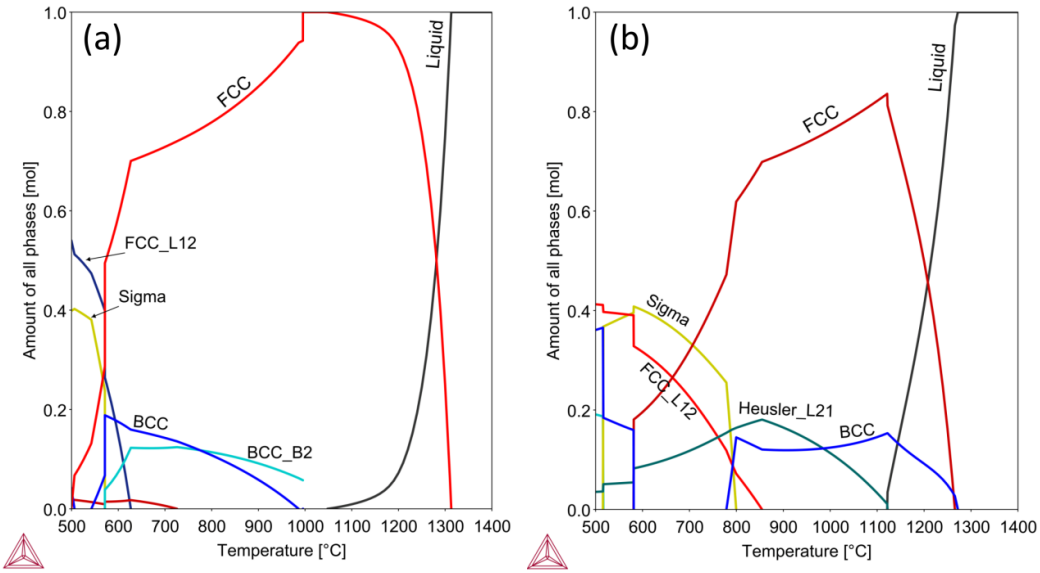

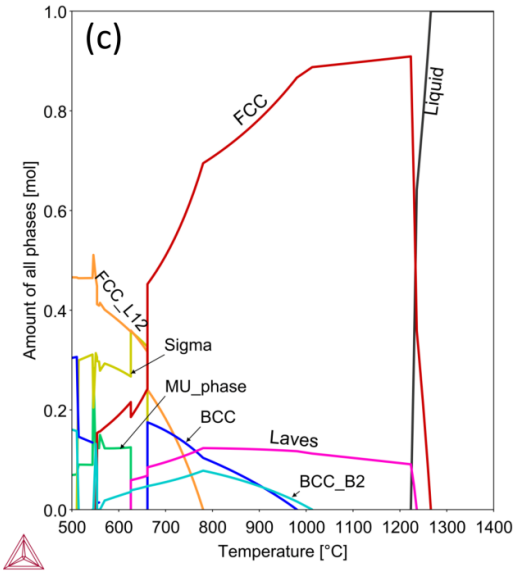

Fig. 1 Equilibrium phase calculation of HEAs by Thermo-calc with the database TCHEA4, (a) HEA-Cu, (b) HEA-Ti, (c) HEA-Nb. (FCC: dis-ordered FCC; FCC_L12: ordered FCC; BCC: dis-ordered BCC; BCC_B2: ordered BCC; SIGMA: σ-phase; MU_phase: μ phase).

3.2 Characterization of as cast alloys

3.2.1 Phase composition

Fig. 2 shows the phase compositions of as cast alloys measured by XRD. Based on the collected results, only the signal of FCC (face-centered cubic) phase is obtained from pristine HEA-Cu, which means the formation of single FCC solid solution in the alloy matrix. Sample HEA-Ti not only shows the evidence of FCC phase, but also the signals of BCC solid solution and B2-Ni(Al,Ti) (ordered BCC) phases have been identified. The peaks positions (2θ) of the BCC and B2 (B2-NiAl, B2-Ni(Al,Ti)), which are related to the lattice planes (110) at ~44.5˚, (200) at ~65˚, and (211) at ~82˚, are separated by less than 1˚. Moreover, the diffraction peak of the B2 phase shifts to lower 2θ due to Ti addition, which indicates the formation of B2-Ni(Al,Ti). The sample with Nb addition (HEA-Nb) maintains FCC phase in the bulk alloy, while additional peaks from Laves have been detected as well. Table 3 summarizes the phases identified on each sample by XRD.

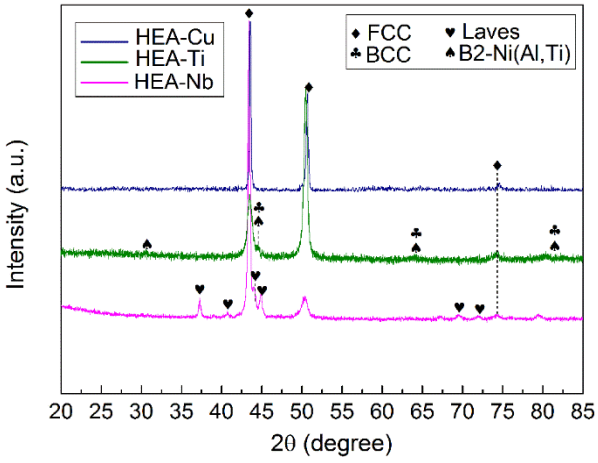

Fig. 2 XRD spectra of HEAs (HEA-Cu, HEA-Ti, HEA-Nb) in as cast condition.

Table 3
Phase compositions of HEAs in as cast state, measured by XRD.

Sample	FCC (33-397)	B2-Ni(Al,Ti) (71-5898)	Laves (17-908)	BCC (34-396)
HEA-Cu	+	-	-	-
HEA-Ti	+	+	-	+
HEA-Nb	+	-	+	-

PDF no. is given in brackets.

3.2.2 Morphologies of bulk alloys

Fig. 3 presents SEM images of the bulk alloys of all HEA samples. HEA-Cu has formed large grains with grain size around 100 to 500 µm, see Fig. 3 (a). Previous XRD measurement reveals the single FCC phase formed in the bulk alloy. However, nano-sized Cu precipitates as found in differently produced alloys with higher Cu content cannot be excluded due to the limited resolution of XRD and SEM [32-34]. In addition, some round and dark precipitates displayed in the image are alumina particles formed during alloy production. The other two alloys HEA-Ti and HEA-Nb have formed dendrite (D) and inter-dendrite (ID) morphologies in the alloy matrix, shown in Fig. 3 (b,c). EDX measurement of the IDs in HEA-Ti shows the enrichment of Al, Ni and Ti (see Table 4), which indicates the B2-Ni(Al,Ti) phase identified by XRD. In addition, the bright stick type structures embedded into the dark regions, are regions enriched in Fe and Cr, which are attributed to the BCC phase. In case of HEA-Nb, the IDs are highly enriched in Nb (see Table 4), which is assigned to the Fe_2Nb Laves phase according to XRD analysis. In addition, a low amount of dark precipitates, which are conjoint with the Laves phase, have been observed and displayed at high magnification image in Fig. 3 (c). According to the EDX evaluation, the chemical compositions are close to the stoichiometric ratio of B2-NiAl, which could be assigned to B2-NiAl phase. However, it is unable to be identified by XRD due to its low fraction (< 5 vol.%).

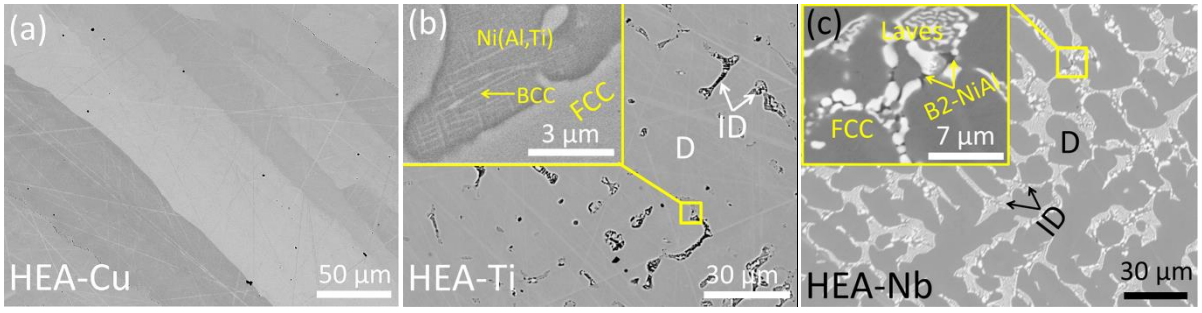

Fig. 3 Representative SEM images of the microstructure of as cast HEAs (HEA-Cu, HEA-Ti and HEA-Nb), D: dendrite; ID: inter-dendrite.

Table 4
Chemical compositions of as-cast HEAs, measured by EDX (at.%).

Alloy	Morphology	Al	Cr	Fe	Ni	Cu	Ti	Nb
HEA-Cu	SP	7.5	22.2	31.8	32.8	5.7	--	--

HEA-Ti	D	6.5	23.9	35.8	31.1	--	2.7	--
	ID	21.1	12.1	16.3	38.3	--	12.2	--
HEA-Nb	D	7.1	23.2	34.4	34.1	--	--	1.2
	ID	6.2	19.5	26.7	30.8	--	--	16.8

SP: single phase; D: dendrite; ID: inter-dendrite. --: without addition of alloying element.

3.2.3 Hardness

The hardness of the designed HEAs is used as a hint of the influence of the alloying elements on the mechanical properties of candidate alloys. Fig. 4 shows the measured Vickers hardness of HEA samples at room temperature. Two other alloys, HEA-ref and SS316 austenitic steel, are used as references. HEA-ref with single FCC phase [30] shows the hardness lower than SS316. By adding Cu, the hardness of HEA-Cu increases by around 12.5% when compared with HEA-ref, but it is still lower than the value of SS316. However, the other two samples with Ti or Nb addition show a hardness 50.3% respectively 56.5% higher than that of SS316.

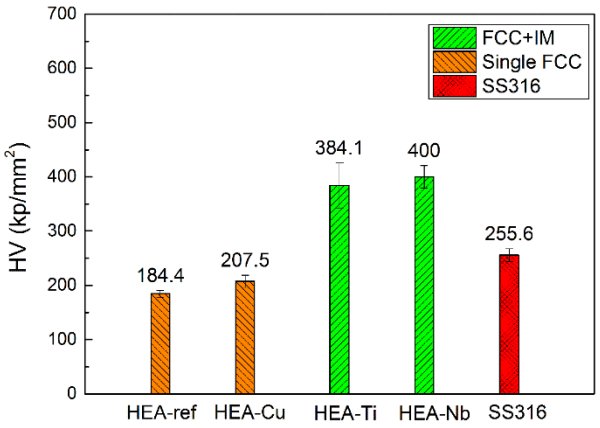

Fig. 4 Vickers hardness measurement of candidate HEAs (HEA-Cu, HEA-Ti, HEA-Nb); HEA-ref and SS316 used as references; HEA-ref: $Al_8Cr_{23}Ni_{35}Fe_{34}$ (at.%).

3.3 Corrosion behaviour

3.3.1 Phase compositions

Fig. 5 (a, b) shows the phase compositions of the surfaces of the HEA samples after the corrosion tests. After 1000 h exposure, the phases obtained from HEA-Cu include FCC (dominant phase), BCC and B2-NiAl phase plus the oxides of Cr_2O_3, spinel-type $Fe(Cr,Al)_2O_4$ and Al_2O_3.

A detailed analysis of HEA-Ti with 1000 h exposure indicates that the main oxides formed are TiO_2 (Rutile) and $TiAl_2O_5$ (Tialite). In addition, the main metallic phase is FCC while σ-phase (FeCr), B2-Ni(Al,Ti), BCC and η-phase (Ni_3Ti) have been identified as well. After 2000 h exposure, signals obtained from oxide phases include $PbTiO_3$, Cr_2O_3 and Al_2O_3 (weak), which is different from the oxides observed after 1000 h exposure. However, the phases from metallic phase or compounds do not change by prolonging the exposure time.

The phase composition of HEA-Nb after 1000 h exposure consists of Cr_2O_3, $(Al,Cr)_2O_3$, FCC phase, Laves, B2-NiAl and Ni_3Nb δ-phase (orthorhombic $D0_a$ structure). These phases are also detected on the samples after 2000 h exposure. In addition, Lead Niobium oxide is also identified on the sample after 2000 h exposure.

All of the identified phases and the corresponding PDF no. have been summarized and given in Table 5.

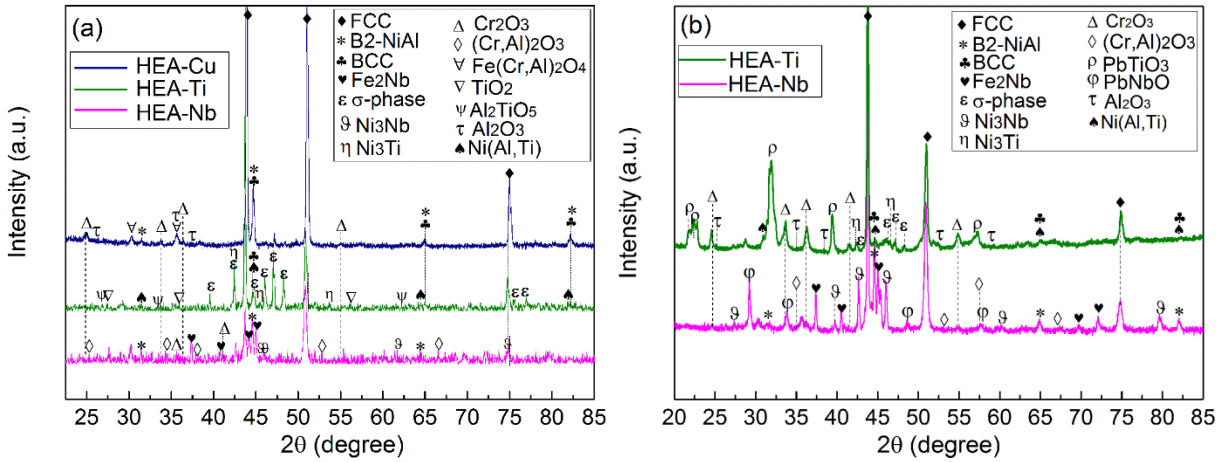

Fig. 5 XRD spectra of HEAs (HEA-Cu, HEA-Ti, HEA-Nb) after 1000 h (a) and 2000 h (b) exposure to molten Pb.

Table 5
Phase compositions of HEAs after corrosion tests, measured by XRD.

Sample	Time	Phase composition[1)]						
	(h)	FCC (33-397)	B2-Ni(Al,Ti) (71-5898)	Laves (17-908)	Other metallic phases	Cr_2O_3 (74-326)	$(Cr,Al)_2O_3$ (77-2188)	Other oxides
HEA-Cu	1000	+	-	-	BCC, B2-NiAl	+	-	$Fe(Cr,Al)_2O_4$ Al_2O_3
HEA-Ti	1000	+	+	-	BCC σ-phase, η-phase	-	-	TiO_2, $TiAl_2O_5$
	2000	+	+	-	BCC, σ-phase, η-phase	+	-	$PbTiO_3$, Al_2O_3
HEA-Nb	1000	+	-	+	B2-NiAl, δ-phase	+	+	
	2000	+	-	+	B2-NiAl, δ-phase	+	+	PbNbO

[1)] PDF no. is given in brackets.

3.3.2 Surface morphologies

The surface morphologies of all exposed samples have been characterized by SEM, shown in Fig. 6.

The surface of HEA-Cu is partially covered by an oxide scale, in which O, Al and Cr are enriched as confirmed by EDX analysis. Besides, protrusions are grown above the Al- and Cr-rich layer. EDX measurement indicates the high concentrations of O, Cr and Fe at the protrusions regions. However, some regions show exfoliation of the oxide scale, with 30% to 40% of surface area on one side, and more than 50% on the other side of the sample, shown in Fig. 6 (a,d). EDX quantative measurements indicate that the chemical compositions at the oxide scale spalled regions are close to the nominal compositons of the bulk alloy, which means no leaching of alloying elements from the bulk alloy take place after the oxide scale spalled off.

HEA-Ti has been passivated by an oxide layer without the evidence of exfoliation. The surface shows similar “inter-dendrite” morphologies as observed in the matrix of the as cast alloy (see Fig. 3 (b) and Fig. 6 (b)). The regions shown in bright contrast are enriched in O and Ti as confirmed by EDX measurement. In contrast, the dark regions in Fig. 6 (b) are rich in O, Al and Cr. After 2000 h exposure, the alloy surface exhibits similar aspects as the sample after 1000 h exposure. In addition, some bright precipitates are distributed on the surface, see Fig. 6 (e). EDX measurement of the chemical compositions indicates that O, Ti and Pb are concentrated at the precipitates.

In case of the alloy with Nb addition (HEA-Nb), the sample surface also displays “dendrite” and “inter-dendrite” structure after corrosion tests, shown in Fig. 6 (c, f). However, an oxygen-rich layer has been confirmed by EDX measurement which is not detected on the sample before the corrosion test (Fig. 3 (c)). According to the EDX analysis, the bright “inter-dendrite” regions are rich in O, Al and Nb while the dark dendrites contain more O, Al and Cr. Compared with the sample after 1000 h exposure, the sample after 2000 h exposure shows enrichment of O, Al, Nb and Pb at the bright “inter-dendrite regions”. The Pb-rich bright precipitates in the image are most probably due to the formation of PbNbO according to XRD measurement. The dark regions are rich in O, Al and Cr.

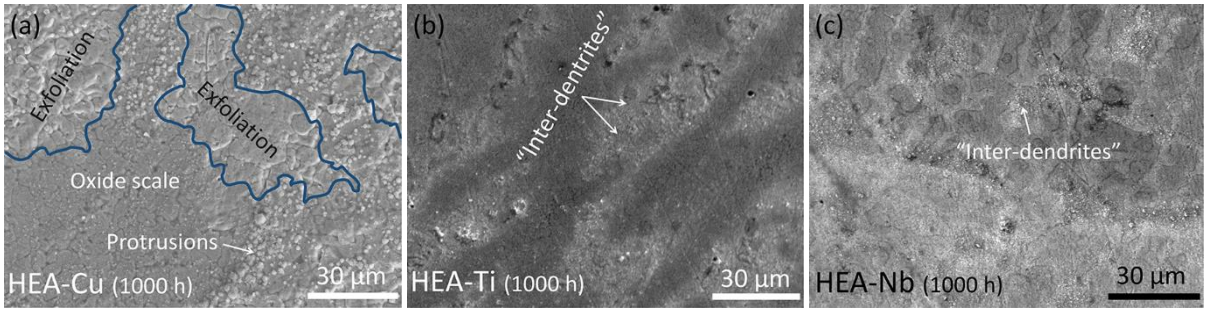

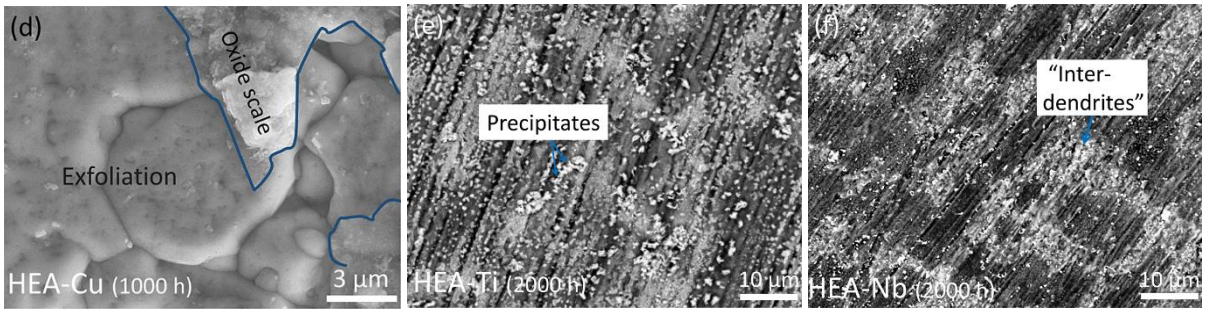

Fig. 6 Surface morphologies of HEA samples (HEA-Cu, HEA-Ti and HEA-Nb) after 1000 h and 2000 h exposure to 10^{-6} wt.% oxygen containing molten Pb at 600 °C.

3.3.3 Cross section analysis

The corrosion behaviour of candidate HEAs has been further characterized through cross section analysis.

HEA-Cu

Fig. 7 presents the cross sectional EDX mapping of HEA-Cu after 1000 h exposure. The sample surface is partially covered by an oxide layer with non-uniform thickness. According to the elemental mapping, the thick part of the oxide scale consists of O, Cr and Fe. Close to the Ni-plate enrichments of O, Cr and Fe are detected, indicating partial detachment of the oxide scale. Below the thick oxide layer, a continuous thin layer with intensified signals of O and Al is observed. It indicates the formation of an alumina layer. An EDX line scan through the oxide scale (Fig. 8 (a)) confirms that O, Cr and Fe (low) are enriched the outer thick layer (layer I) with a thickness around 0.3 to 0.5 µm, which is consistent with the composition of protrusions observed from SEM surface image (Fig. 6 (a)). Further measurement at the inner part of the oxide scale (Layer II) shows a narrow region highly concentrated in Al, which is also indicated in EDX mapping. The thickness of the Al-rich thin oxide layer is around 90 nm according to the full width at half maximum (FWHM) of the measured EDX signal. The formation of $Fe(Cr,Al)_2O_4$ spinel layer results in the reduced oxygen activity at the interface of oxide scale/alloy matrix, which only allows Al to be oxidized due to the lowest oxygen dissociation partial pressure of Al_2O_3 [30-31]. Moreover, an increased intensity of the Cu signal has been detected underneath the Al- and O-rich layer, which is also confirmed by several measurements at different regions. Another EDX line scan is performed at the region where the oxide scale spalled off, shown in Fig. 8 (b). According to the elemental profiles, no increased signals of O, Al and Cr are detected on the metal surface. The measured chemical compositions in alloy matrix are comparable to that of as cast alloy. Neither corrosion attack nor selective leaching of Ni has been observed in the bulk alloy. This observation supports the statement that the oxide scale exfoliation happened after the corrosion test, for instance during the cooling process, due to poor scale adherence.

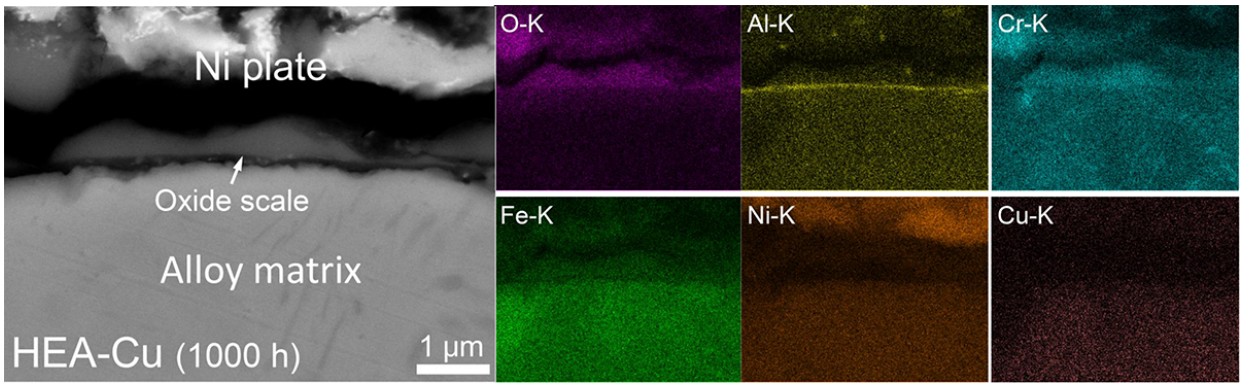

Fig. 7 SEM-EDX elemental mapping of the cross section of HEA-Cu after 1000 h exposure to 10^{-6} wt.% oxygen containing molten Pb at 600 °C.

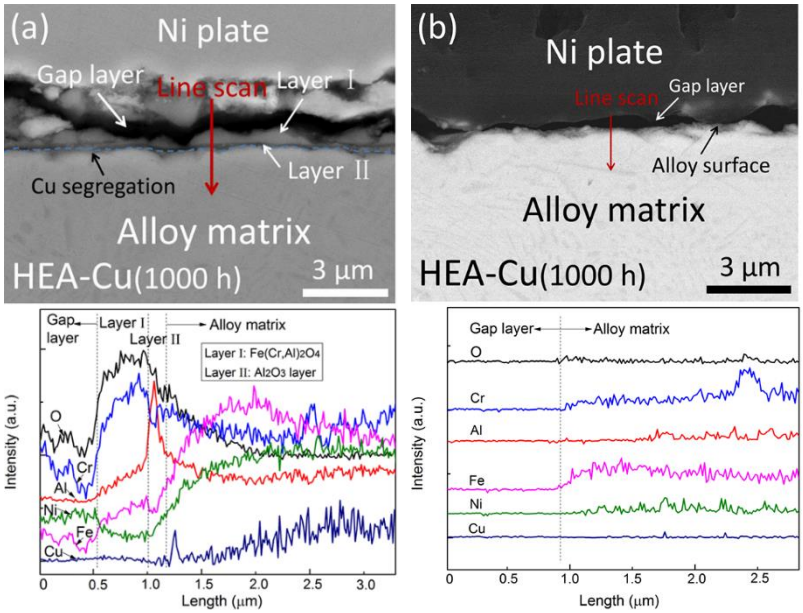

Fig. 8 SEM-EDX line profiles of the cross section of HEA-Cu after 1000 h exposure to 10^{-6} wt.% oxygen containing molten Pb at 600 °C, (a) sample surface covered by oxide scale, (b) sample surface without oxide scale. Gap layer: a gap between the Ni-plate and oxide scale.

HEA-Ti

Fig. 9 shows the SEM-EDX mapping of the cross section of HEA-Ti after 1000 h exposure. The sample surface is covered by a continuous oxide layer. According to the EDX elemental mapping, coincided signals maxima of O, Al and Ti have been detected in the oxide scale region. Besides, the oxide layer at some spots is thicker than elsewhere, marked in Fig. 9. An EDX measurement shows that O, Cr, Fe and Ti are detected at these parts. The total thickness of the oxide scale varies from 0.5 to 0.9 μm. Further measurement has been performed by the EDX line scan, shown in Fig. 10 (a). The signal of Ni obtained above the oxide layer (in the gap layer region), where the O signal is absent, are from the deposited Ni-layer. In the oxide scale region, coincided signals of O, Ti and Fe are detected at the outer part of the scale, indicating the formation of oxides mixture. In addition, strong signals from O, Cr and Al are mainly present

at the inner part of the layer. Below the oxide layer, the compositions variation is mainly due to the formation of different phases like B2-NiAl, σ-phase (Fe-, Cr- rich) or η-phase (Ni-, Ti- rich) in alloy matrix.

Fig. 10 (b) shows the line profiles of the cross section of HEA-Ti after 2000 h exposure. The oxide layer formed with prolonged exposure time presents different features compared with the sample after 1000 h exposure, namely, thick oxidized part, and a severely deformed oxide scale. The thickness of the oxide scale region varies from 3.0 µm to 6.0 µm, much thicker than the oxide layer formed after 1000 h exposure. Moreover, a continuous layer shown in dark contrast has formed at the inner part of the layer. Further EDX line scan measurement of the outer part of the scale shows the mixed signals from O, Al, Cr, Ti, Fe and even Pb, indicating the formation of mixed oxide layer. As the measurement reaches the inner dark layer part, a signal maximum of Al is visible coinciding with a high O intensity. This result indicates that the inner layer could be composed of Al_2O_3. The Pb signal detected at the outer layer is invisible at the inner Al_2O_3 layer, indicating the efficient role of alumina scale as a diffusion barrier.

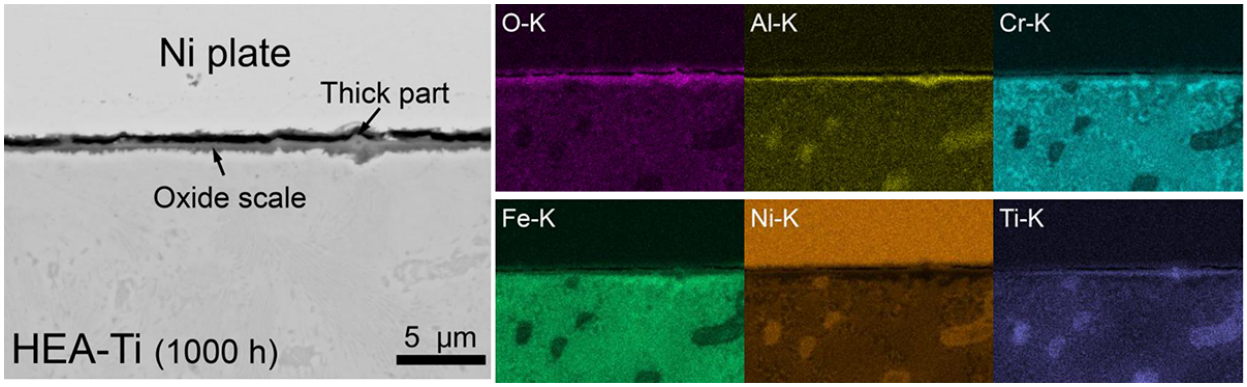

Fig. 9 SEM-EDX elemental mapping of the cross section of HEA-Cu after 1000 h exposure to 10^{-6} wt.% oxygen containing molten Pb at 600 °C.

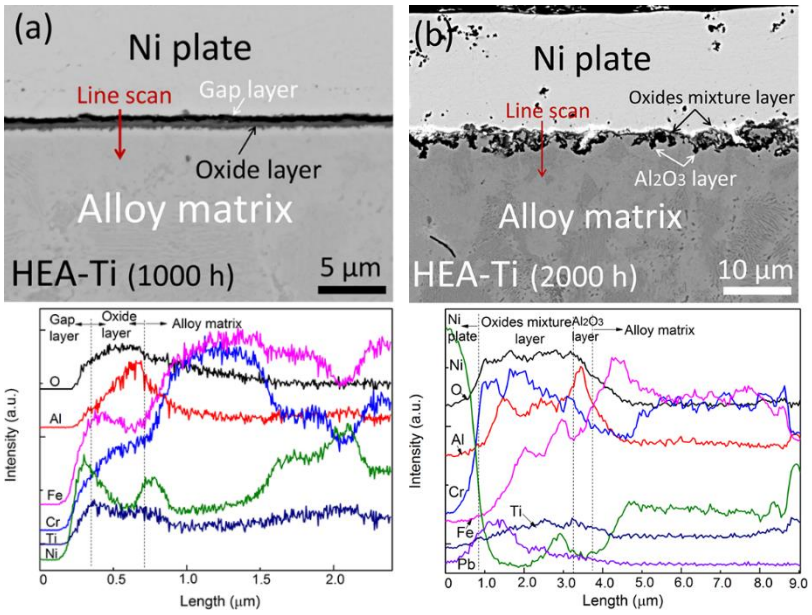

Fig. 10 SEM-EDX line profiles of the cross section of HEA-Ti after 1000 h (a) and 2000 h (b) exposure to 10^{-6} wt.% oxygen containing molten Pb at 600 °C; Gap layer: a gap between the Ni-plate and oxide scale.

HEA-Nb

Fig. 11 shows the cross sectional SEM-EDX mapping of HEA-Nb after 1000 h exposure. A continuous oxide scale, mainly consisting of O and Al, is observed on the alloy surface. The general thickness of the oxide scale is around 0.2 µm. At the region below the oxide scale, enrichment of Fe and Cr has been observed. The EDX line scan in Fig. 12 (a) also confirms the measurement of EDX mapping, namely O, Cr and Al enrichment at the oxide layer region. Below the oxide layer, a discontinuous bright region enriched in Fe and Ni, also called transitional layer (TL) [10], has formed at Laves-phase free regions, see Fig. 12 (a). Beside, some Cr-rich precipitates are also visible in the TL. The thickness of TL reaches up to 2.5 µm in depth. After 2000 h exposure, the passivating oxide scale on the sample surface presents similar features as observed on the sample after 1000 h exposure, namely a thin oxide layer mainly enriched in O, Cr and Al, and a TL at the Laves free regions, shown in Fig. 12 (b). The signals of Cr and Al become separated where Cr signal is located at the outer part while Al signal is in the inner part. The measured thickness of oxide scale is around 0.4 µm. Moreover, as the exposure time increases, the intensity of Al signal is increased in the inner layer. In addition, a slight increase of Pb signal combined with the signals from Nb, Fe, Cr, Ni and O, which is detected above laves phase region (Fig. 12 (b)) after 2000 h exposure, further confirms the formation of Pb-rich oxides at the "bright inter-dendrites" regions, see Fig. 6 (f). The thickness of Pb-containing oxide scale region is around 0.5 µm, which is slightly thicker than the general oxide layer part.

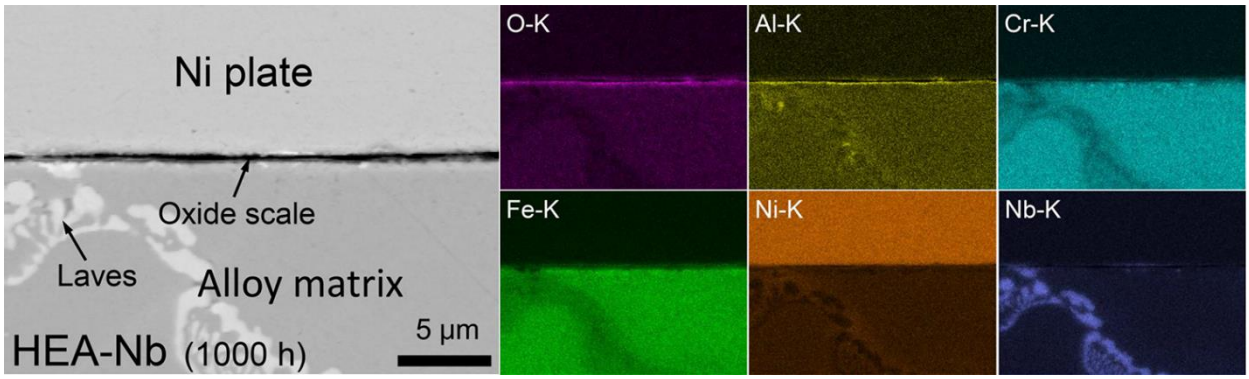

Fig. 11 SEM-EDX elemental mapping of the cross section of HEA-Nb after 1000 h exposure to 10^{-6} wt.% oxygen containing molten Pb at 600 °C.

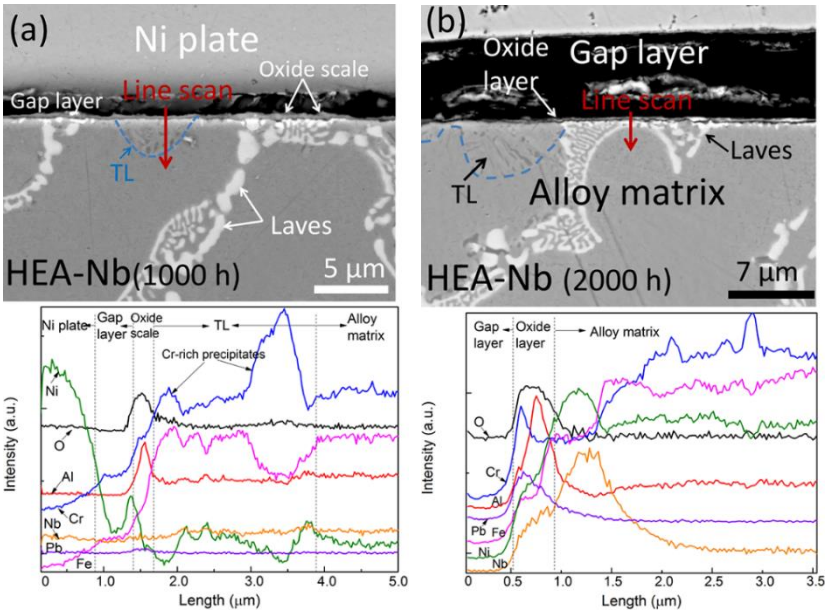

Fig. 12 SEM-EDX line profiles of the cross section of HEA-Nb after 1000 h (a) and 2000 h (b) exposure to 10^{-6} wt.% oxygen containing molten Pb at 600 °C; Gap layer: a gap between the Ni-plate and oxide scale.

3.5 Bulk alloy microstructure evolution

Fig. 13 (a) presents the bulk alloy morphologies of HEA samples after 1000 h exposure. The phase compositions are identified by the XRD, which are displayed in Fig. 5 and Table 5. According to the XRD measurements (Fig. 5 (a)) and EDX analysis, the bulk alloy is able to preserve FCC dominant matrix, marked in Fig. 13 (a). In addition, rod type nano-sized precipitates, shown in dark contrast, are distributed in the whole alloy matrix. EDX measurement of the precipitates indicate the enrichment of Al and Ni. The bright lamellae layer between the dark precipitates are rich in Cr and Fe. Combining with the XRD result (in Fig. 5 (a)), the dark precipitates are assigned to the identified B2-NiAl phase while the bright region is BCC phase.

The microstructure of the alloy matrix of HEA-Ti after 1000 h exposure is shown in Fig. 13 (b). Generally, three types of morphologies have been recognized in the bulk alloy. The first type are large and dark precipitates, which are enriched in Al, Ni and Ti, as measured by EDX analysis. This type of precipitates are the same as the inter-dendrites in the as cast alloy, which belong to B2-Ni(Al,Ti) and BCC phase. The second type displays the stick-type morphologies, distributed in the whole image. EDX line scan measurement shows the segregation of Ni and Ti at the stick structure. The microstructure of these precipitates fits the characteristics of η-phase [63], which is also confirmed by XRD analysis. The third type is the large bright area with two different contrasts (dark and bright areas), which is more visible after 2000 h exposure, shown in Fig. 13 (d). Further EDX analysis (mapping, point measurement) has shown the enrichment of Cr at the dark area, which can be the σ-phase identified by XRD. The bright areas are rich in Ni, which is a FCC stabilizer, and therefore these are attributed to the remaining FCC alloy matrix. Compared with the sample after 1000 h exposure, the phase compositions in alloy matrix do not change after 2000 h exposure, namely FCC, B2-Ni(Al,Ti), BCC, η-phase and σ-phase.

The microstructure of HEA-Nb with 1000 h exposure is shown in Fig. 13 (c). The main structure in the bulk alloy includes FCC solid solution matrix plus inter-dendrites of Laves as well as conjoint B2, which are also observed in the pristine alloy. In addition, some bright precipitates (less bright than Laves) are found at regions adjacent to the Laves-phase inter-dendrites, marked in Fig. 13 (c). Concurrent with the XRD (Fig. 5) and EDX measurement, these precipitates belong to Ni_3Nb δ-phase. The δ-phase is reported to nucleate in Ni-based alloys in terms of ribbon or plate like morphologies [58, 64]. After 2000 h exposure, the sample presents similar morphologies as that observed after 1000 h exposure, namely FCC alloy matrix plus secondary phases of Laves, B2 and δ-phase. In addition, needle/acicular like precipitates adjacent to the inter-dendrites are also observed, shown in Fig. 13 (e). EDX measurement shows that the precipitates are enriched in Al and Ni, which are consistent with the B2-NiAl phase detected by XRD.

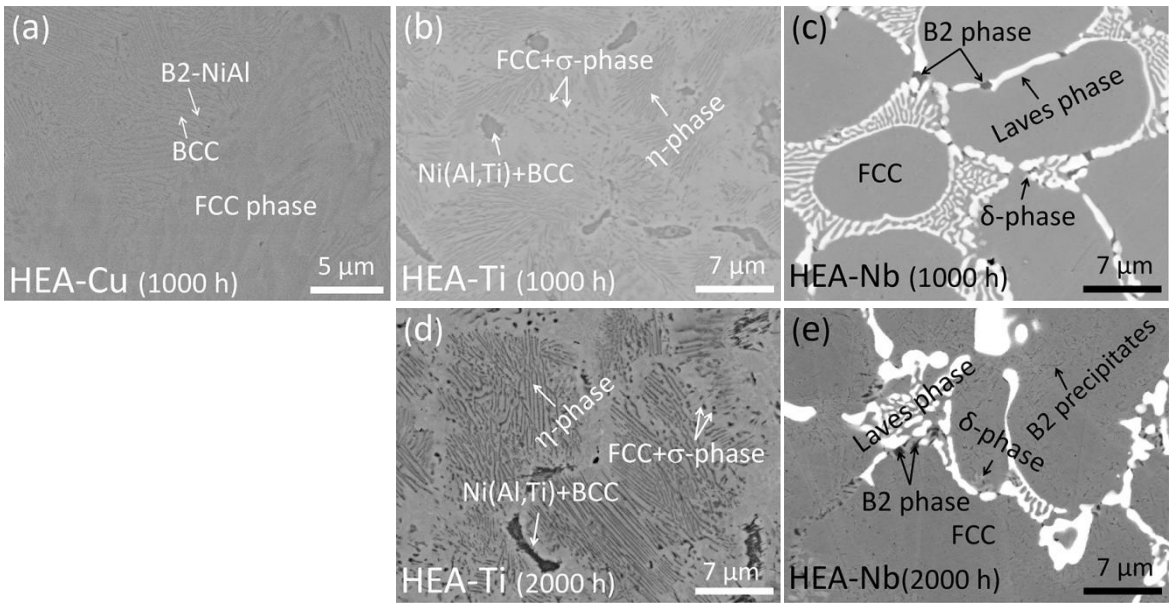

Fig. 13 Morphologies of the bulk alloy of HEA samples after 1000 h (a, b, c) and 2000 h (d, e) exposure at 600 °C.

4. Discussion

4.1 Effects of alloying elements on phase formation and hardness of as cast alloys

The sample alloyed with Cu has formed single FCC solid solutions in the as cast alloy. The results of microstructure characterizations have confirmed the alloy design approach, which also indicate the role of Cu in stabilizing the FCC phase. The sample with Ti addition has formed B2-Ni(Al,Ti) and BCC phases in addition to the FCC matrix. The formation of B2-Ni(Al,Ti) phase is mainly due to the relatively low enthalpy of formation of (Al,Ti) with Ni [65-66]. Moreover, spinodal decomposition happens within the inter-dendrites due to the segregations of Ni, Al and Ti, which leads to the formation of Fe-, Cr-rich BCC phase [67-68]. Adding Nb promotes the formation of Nb-rich Laves in HEA-Nb. In addition, small amounts of B2-NiAl phase, which are conjoint with Laves phase, have been identified. Since the formation of Fe- and Nb-rich Laves phase repels additional Ni and Al, local enrichment of Ni and Al can lead to the formation of B2-NiAl inter-metallic compound at adjacent locations [57-58].

Hardness measurement of designed alloys indicates that Ti and Nb have significant beneficial effects on the strengthening properties of HEAs. This is mainly due to precipitation of strengthening phases like B2 or/and Laves [35-36]. The strengthening effect of Cu addition is very limited. Alloying Cu is reported to either dissolve in the alloy matrix or segregate as Cu-rich FCC phase, which helps to improve the ductility of the base alloy [69-70].

4.2 Effects of alloying elements on corrosion behaviour

The thickness of the oxide scale formed on the three HEAs with different exposure time is summarized in Table 6. According to the results, both Cu and Ti additions degrade the oxidation/corrosion resistance of HEAs either by oxide scale exfoliation or formation of thick oxide layer. The accelerated oxidation of HEA-Ti with prolonged exposure time is due to the formation of a fast growing Ti-rich oxides scale with lower protection capabilities [31, 71]. In contrast, the sample with Nb addition has formed a thin layer, with relatively low oxidation rate.

Table 6
Thickness of oxide scale formed on HEAs with different exposure time.

Code	Thickness (μm)	
	1000 h	2000 h
HEA-Cu	0.4-0.6 (partial spallation)	--
HEA-Ti	0.5-0.9	3.0-6.0
HEA-Nb	~0.2	0.4

--: no experimental data.

The influences of Cu addition on the corrosion behaviour can be discussed from two points of view. Firstly, compared with the Cu-free sample (HEA-ref), the sample with Cu addition has formed a thick outer layer of $Fe(Cr,Al)_2O_4$ instead of thin Cr_2O_3 layer. Although results from literature have indicated that Cu addition decreases the oxidation rate of Fe-Ni-Cr-Al austenitic alloys and AlCoCrCuxFeNi (x: 0, 0.5, 1) during the early stage of exposure [37, 40], the observed results from this study show the negative influence of Cu addition on the oxidation rate. This is mainly due to the faster growth rate of $Fe(Cr,Al)_2O_4$ layer when compare with Cr_2O_3 layer [15]. The fast growth rate can be associated with the higher diffusion rates of oxygen (inward) and alloying elements (outward). Secondly, the oxide scale adherence is degraded by alloying with Cu, which is also observed by other researchers [38-39]. The Cu-segregated layer might create a diffusion barrier for oxygen penetration and outward diffusion of passive oxide layer formers like Al and Cr. It can be deduced that the bonding strength at the interface of oxide scale/alloy matrix is significantly reduced by Cu segregation.

Ti addition degrades the corrosion resistance of Al-Cr-Fe-Ni HEA alloy when exposed to molten Pb. The corrosion behaviour of HEA-Ti is consistent with reported results [31, 44, 46]. Instead of forming slowly growing alumina rich oxide scale on alumina forming alloys, less protective Ti-rich oxide mixtures are formed by alloying with Ti. The fast diffusion of oxygen and alloying elements results in the formation of thick oxide scale [73]. Also, Ti addition increases the solubility of oxygen in the alloy matrix, which promotes internal Al oxidation [74]. Moreover, Pb reacts with TiO_2 to form $PbTiO_3$ oxide at high

temperature [75], which is also identified in this study. As the thickness of oxides mixture layer increases with prolonged exposure time (from 1000 h to 2000 h), the oxygen activity at the oxide scale/bulk alloy interface will be decreased. As soon as the oxygen oxygen activity is reduced to a certain level, it only allows Al to be oxidized because of the lowest oxygen dissociation partial pressure of Al_2O_3 [30-31].

In case of the sample with Nb addition, the alloy exhibits promising corrosion resistance by forming protective oxide scale based on Al_2O_3 and Cr_2O_3, where more Al_2O_3 has formed at the inner part and a segregation of Cr_2O_3 and Al_2O_3 are observed with prolonged exposure. The study of Nb containing alumina-forming alloys indicates that adding Nb not only increases the Cr solubility in austenite, but also reduces the oxygen solubility in alloy matrix [76]. Both are favorable for the external alumina scale formation. In addition, Fe_2Nb Laves phase itself also acts as a reservoir for alumina scale formation because of high solubility of Al (up to 50 at.%) in Laves [31, 77]. Even Al_2O_3 can grow on Laves phase. The observed TL below the oxide scale is a result of elemental diffusion caused by the oxidation process, which is also observed in alumina-forming austenitic alloys [10].

4.3 Microstructure stability during exposure

HEA-Cu has experienced phase transformation after 1000 h exposure. Both experiments and equilibrium phase calculation of HEA-Cu confirm the formation of B2 and BCC phase at 600 °C in addition to the FCC phase already obtained for the as cast alloy. It is reported that Cu tends to segregate as the Cu-rich FCC phase [78]. This can lead to the local enrichment of BCC stabilizers like Fe and Cr, which promote the formation of BCC phase. Moreover, a local enrichment of Al and Ni promotes the formation of B2-NiAl phase because of the low enthalpy of formation (-22 kJ/mol calculated by Miedema's model [79]).

The microstructure of HEA-Ti is unstable during thermal aging. In addition to B2-Ni(Al,Ti) and BCC phases already obtained in the cast alloy, σ-phase and η-phase precipitates have been observed after exposure. The precipitation of B2-Ni(Al,Ti) phase is beneficial for the high temperature creep strength [79]. However, this meta-stable phase can transform to another meta-stable γ'-phase (Ni_3(Al,Ti)) at elevated temperature [80], which usually increases the ductility of the base alloy. The γ'-phase can further transform to the brittle η-phase at the exposed temperature [81], as identified in this study. Some strategies have been proposed to improve the thermal stability of γ'-phase. For instance, increasing the Al amount in $Al_xCo_{1.5}CrFeNi_{1.5}Ti_y$ (x+y=0.5) can suppress the γ'→η phase transformation up to 900 °C [81]. Regarding σ-phase, the local depletion of Ni due to the formation of B2-Ni(Al,Ti) and η phase can result in the enrichment of Cr and Fe, which might promote the formation of σ-phase.

The phase compositions of exposed HEA-Nb (after 1000 h, 2000 h exposure) do not fit the equilibrium phase calculation results presented in Fig. 1 (c) very well. Instead of the predicted secondary phases like σ-phase, BCC_B2 (B2-NiAl) and MU_phase (see in Fig. 1 (c) at 600 °C), the Laves, B2-NiAl and Ni_3Nb δ-phase (orthorhombic $D0_a$ structure) have been identified after 1000 and 2000 h exposure. The δ-phase is reported to reduce the strength of base alloys [64]. However, it is beneficial to the grain stabilization and stress rupture properties of bulk alloy by careful controlling distributions of δ-phase [64]. The Laves phase

is reported to be stable up to 1600 °C [82]. Another type, acicular B2-NiAl precipitates, which are formed due to the local segregation of Al and Ni at regions close to Fe_2Nb inter-dendrites, are also observed in Al-Co-Cr-Fe-Nb-Ni HEAs after thermal aging at 800 to 1000 °C [57-58].

The phase calculation represents an equilibrium stage, while the alloys prepared for the experiment start from an non-equilibrium state (as casting). This might explain the difference in phase compositions between equilibrium phase calculations and experimental observation after exposure (1000 h and 2000 h). However, the equilibrium phase calculation can be used as a guide for the alloy design which might help to avoid the formation of brittle phase like σ-phase.

5. Summary

Based on the results, the main conclusions can be summarized as following:

(a) With the aid of empirical parameters (e.g. ΔH_{mix}, δr, Ω, VEC) and thermo-dynamic calculations, it is possible to design HEAs with single FCC solid solutions ($Al_{8.0}Cr_{22.0}Fe_{32.0}Ni_{33.0}Cu_{5.0}$) and alloys with FCC plus inter-metallic compounds ((B2-Ni(Al,Ti) and BCC, $Al_{7.9}Cr_{22.0}Fe_{31.9}Ni_{33.2}Ti_{5.0}$) or (Laves and B2-NiAl phase, $Al_{8.2}Cr_{21.4}Fe_{30.3}Ni_{35.0}Nb_{5.1}$).

(b) Hardness tests of all three alloys show that Cu addition has slightly increased the hardness of Al-Cr-Fe-Ni based HEA, while Ti or Nb addition can significantly improve the hardness because of the precipitation of strengthening phases.

(c) Cu addition has negative influence on the corrosion/oxidation behaviour of Al-Cr-Fe-Ni based HEA at 600 °C. On one hand, HEA-Cu has formed thick oxide layer based on an outer layer of $Fe(Cr,Al)_2O_4$ and an inner layer of Al_2O_3. On the other hand, the passive oxide scale shows poor scale adherence due to Cu addition. A Cu segregated layer has been observed between the oxide layer and alloy matrix, which might degrade the bonding strength of oxide scale.

(d) The corrosion/oxidation resistance of Al-Cr-Fe-Ni model alloy is also degraded by alloying with Ti. HEA-Ti has formed TiO_2 and $TiAl_2O_5$ layer after 1000 h exposure, while an outer layer of $PbTiO_3$, Cr_2O_3 and an internal layer of Al_2O_3 has been observed after 2000 h exposure. The formation of continuous Al_2O_3 layer can effectively inhibit the inward penetration of liquid Pb.

(e) Nb addition shows beneficial effects on the corrosion/oxidation behaviour of Al-Cr-Fe-Ni based HEAs. A thin oxide scale based on Cr_2O_3 and Al_2O_3 has formed after 1000 h exposure, and more Al_2O_3 is detected in the oxide scale as exposure time increases.

(f) Microstructure investigation of exposed HEA samples show that new phases like BCC and B2-NiAl have formed in HEA-Cu after 1000 h exposure. HEA-Ti has experienced phase transformations including the formation of σ-phase and η-phases after 1000 h and 2000 h exposure. Regarding HEA-Nb sample, $NbNi_3$ δ-phase has been identified after 1000 h while additional acicular B2 precipitates are observed after 2000 h exposure.

Alloying elements like Cu, Ti and Nb do not only influence the microstructure of as cast HEA alloys, but also cause significant effects on the corrosion behaviour and microstructure stability. Adding Cu or Ti

can degrades the corrosion/oxidation resistance of Al-Cr-Fe-Ni HEA alloys in oxygen-containing molten Pb, although the corrosion resistance of Ti-containing HEA alloy is still acceptable. Alloying with Nb, the corrosion/oxidation resistance of Al-Cr-Fe-Ni HEA model alloy has been improved, in terms of forming protective Cr_2O_3/Al_2O_3 bi-layer. However, when we consider the microstructure stability of all designed alloys at higher temperatures, it still needs to be improved, especially to avoid the formation of large proportion of brittle phases like σ-phase, δ-phase. Therefore, future work is still needed to improve the microstructure stability, for example by optimizing the chemical compositions or performing dedicated heat treatments.

Data availability

The raw/processed data required to reproduce these findings cannot be shared at this time due to technical or time limitations.

The datasets obtained during the current study are available from the corresponding author on reasonable request.

Acknowledgment

This work is supported by the Helmholtz program NUSAFE at the Karlsruhe Institute of Technology and has been carried out in the frame of EERA Point Programme of Nuclear Materials. Hao Shi appreciates the Postdoc fellowship jointly funded by Helmholtz-OCPC Program (No. 20191028).

References

[1] J.E. Kelly, Generation IV International Forum: A decade of progress through international cooperation, Prog. Nucl. Energy 77 (2014) 240-246, https://doi.org/10.1016/j.pnucene.2014.02.010.

[2] K. Van Tichelen, G. Kennedy, F. Mirelli, A. Marino, A. Toti, D. Rozzia, E. Cascioli, S. Keijers, P. Planquart, Advanced Liquid-Metal Thermal-Hydraulic Research for MYRRHA, Nucl Technol. 206 (2020) 150-163, https://doi.org/10.1080/00295450.2019.1614803.

[3] C. Fazio, V.P. Sobolev, A. Aerts, S. Gavrilov, K. Lambrinou, P. Schuurmans, A. Gessi, P. Agostini, A. Ciampichetti, L. Martinelli, S. Gosse, Handbook on lead-bismuth eutectic alloy and lead properties, materials compatibility, thermal-hydraulics and technologies-2015 edition (No. NEA--7268), Organisation for Economic Co-Operation and Development, 2015.

[4] F. Roelofs, B. de Jager, A. Class, H. Jeanmart, P. Schuurmans, A. Ciampichetti, G. Gerbeth, R. Stieglitz, C. Fazio, European research on HLM thermal hydraulics for ADS applications, J. Nucl. Mater. 376 (2008) 401-404, https://doi.org/10.1016/j.jnucmat.2008.02.014.

[5] J. Pacio, T. Wetzel, Assessment of liquid metal technology status and research paths for their use as efficient heat transfer fluids in solar central receiver systems, Sol. Energy 93 (2013) 11-22, https://doi.org/10.1016/j.solener.2013.03.025.

[6] A. Heinzel, W. Hering, J. Konys, L. Marocco, K. Litfin, G. Müller, J. Pacio, C. Schroer, R. Stieglitz, L. Stoppel, A. Weisenburger, Liquid Metals as Efficient High-Temperature Heat-Transport Fluids, Energy Technol. 5 (2017) 1026-1036, https://doi.org/10.1002/ente.201600721.

[7] H. Kim, D. Boysen, J. Newhouse, B. Spatocco, B. Chung, P. Burke, D. Bradwell, K. Jiang, A. Tomaszowska, K. Wang, W. Wei, L. Ortiz, S. Barriga, S. Poizeau, D. Sadoway, Liquid metal batteries: past, present, and future, Chem. Rev. 113 (2013) 2075-2099, https://doi.org/10.1021/cr300205k.

[8] G. Müller, A. Heinzel, J. Konys, G. Schumacher, A. Weisenburger, F. Zimmermann, V. Engelko, A. Rusanov, V. Markov, Behavior of steels in flowing liquid PbBi eutectic alloy at 420–600 ˚C after 4000–7200 h, J. Nucl. Mater. 335 (2004) 163-168, https://doi.org/10.1016/j.jnucmat.2004.07.010.

[9] J. Zhang, A review of steel corrosion by liquid lead and lead–bismuth, Corros. Sci. 51 (2009) 1207-1227, https://doi.org/10.1016/j.corsci.2009.03.013.
[10] H. Shi, A. Jianu, A. Weisenburger, C. Tang, A. Heinzel, R. Fetzer, F. Lang, R. Stieglitz, G. Müller, Corrosion resistance and microstructural stability of austenitic Fe–Cr–Al–Ni model alloys exposed to oxygen-containing molten lead, J. Nucl. Mater. 524 (2019) 177-190, https://doi.org/10.1016/j.jnucmat.2019.06.043.
[11] J. Van den Bosch, R.W. Bosch, D. Sapundjiev, A. Almazouzi, Liquid metal embrittlement susceptibility of ferritic–martensitic steel in liquid lead alloys, J. Nucl. Mater. 376 (2008) 322-329, https://doi.org/10.1016/j.jnucmat.2008.02.008.
[12] A. Hojna, F. Di Gabriele, J. Klecka, Characteristics and Liquid Metal Embrittlement of the steel T91 in contact with Lead–Bismuth Eutectic, J. Nucl. Mater. 472 (2016) 163-170, https://doi.org/10.1016/j.jnucmat.2015.08.048.
[13] C. Schroer, O. Wedemeyer, J. Novotny, A. Skrypnik, J. Konys, Selective leaching of nickel and chromium from Type 316 austenitic steel in oxygen-containing lead–bismuth eutectic (LBE), Corros. Sci. 84 (2014) 113-124, https://doi.org/10.1016/j.corsci.2014.03.016.
[14] K. Lambrinou, E. Charalampopoulou, T. Van der Donck, R. Delville, D. Schryvers, Dissolution corrosion of 316L austenitic stainless steels in contact with static liquid lead-bismuth eutectic (LBE) at 500 °C, J. Nucl. Mater. 490 (2017) 9-27, https://doi.org/10.1016/j.jnucmat.2017.04.004.
[15] H. Shi, R. Fetzer, C. Tang, D. V. Szabó, S. Schlabach, A. Heinzel, A. Weisenburger, G. Müller, The influence of Y and Nb addition on the corrosion resistance of Fe-Cr-Al-Ni model alloys exposed to oxygen-containing molten Pb, Corros. Sci. 179 (2021) 109152, https://doi.org/10.1016/j.corsci.2020.109152.
[16] A. Heinzel, A. Weisenburger, G. Müller, Long-term corrosion tests of Ti_3SiC_2 and Ti_2AlC in oxygen containing LBE at temperatures up to 700 °C, J. Nucl. Mater. 482 (2016) 114-123, https://doi.org/10.1016/j.jnucmat.2016.10.007.
[17] B. Tunca, T. Lapauw, C. Callaert, J. Hadermann, R. Delville, N.C. El'ad, M. Dahlqvist, J. Rosén, A. Marshal, K.G. Pradeep, J.M. Schneider, J. Vleugels, K. Lambrinou, Compatibility of Zr_2AlC MAX phase-based ceramics with oxygen-poor, static liquid lead–bismuth eutectic, Corros. Sci. (2020) 108704, https://doi.org/10.1016/j.corsci.2020.108704.
[18] J.W. Yeh, S.K. Chen, S.J. Lin, J.Y. Gan, T.S. Chin, T.T. Shun, C.H. Tsau, S.Y. Chang, Nanostructured high-entropy alloys with multiple principal elements: novel alloy design concepts and outcomes, Adv. Eng. Mater 6 (2004) 299-303, https://doi.org/10.1002/adem.200300567.
[19] B. Cantor, I.T.H. Chang, P. Knight, A.J.B. Vincent, Microstructural development in equiatomic multicomponent alloys, Mater. Sci. Eng. A. 375 (2004) 213-218, https://doi.org/10.1016/j.msea.2003.10.257.
[20] B. Gludovatz, A. Hohenwarter, D. Catoor, E.H. Chang, E.P. George, R.O. Ritchie, A fracture-resistant high-entropy alloy for cryogenic applications, Science 345 (2014) 1153-1158, DOI: 10.1126/science.1254581.
[21] Z. Li, K.G. Pradeep, Y. Deng, D. Raabe, C.C. Tasan, Metastable high-entropy dual-phase alloys overcome the strength–ductility trade-off, Nature 534 (2016) 227-230, https://doi.org/10.1038/nature17981.
[22] J.W. Yeh, Recent progress in high-entropy alloys, Ann. Chim. Sci. Mater. 31 (2006) 633–48.
[23] Y. Zhang, T.T. Zuo, Z. Tang, M.C. Gao, K.A. Dahmen, P.K. Liaw, Z.P. Lu, Microstructures and properties of high-entropy alloys, Prog. Mater. Sci. 61 (2014) 1-93, https://doi.org/10.1016/j.pmatsci.2013.10.001.

[24] W.R. Wang, W.L. Wang, S.C. Wang, Y.C. Tsai, C.H. Lai, J.W. Yeh, Effects of Al addition on the microstructure and mechanical property of Al_xCoCrFeNi high-entropy alloys, Intermetallics 26 (2012) 44-51, https://doi.org/10.1016/j.intermet.2012.03.005.
[25] T.M. Butler, M.L. Weaver, Oxidation behavior of arc melted AlCoCrFeNi multi-component high-entropy alloys, J. Alloys Compd. 674 (2016) 229-244, https://doi.org/10.1016/j.jallcom.2016.02.257.
[26] J.C. Rao, H.Y. Diao, V. Ocelík, D. Vainchtein, C. Zhang, C. Kuo, Z. Tang, W. Guo, J.D. Poplawsky, Y. Zhou, P.K. Liaw, J.Th. M.De Hosson, Secondary phases in Al_xCoCrFeNi high-entropy alloys: An in-situ TEM heating study and thermodynamic appraisal, Acta Mater. 131 (2017) 206-220, https://doi.org/10.1016/j.actamat.2017.03.066.
[27] B. Gwalani, V. Soni, M. Lee, S.A. Mantri, Y. Ren, R. Banerjee, Optimizing the coupled effects of Hall-Petch and precipitation strengthening in a $Al_{0.3}$CoCrFeNi high entropy alloy, Mater. Des. 121, (2017) 254-260, https://doi.org/10.1016/j.matdes.2017.02.072.
[28] B. Gwalani, S. Gorsse, D. Choudhuri, Y. Zheng, R.S. Mishra, R. Banerjee, Tensile yield strength of a single bulk $Al_{0.3}$CoCrFeNi high entropy alloy can be tuned from 160 MPa to 1800 MPa, Scr. Mater. 162 (2019) 18-23, https://doi.org/10.1016/j.scriptamat.2018.10.023.
[29] H. Ocken, Reducing the cobalt inventory in light water reactors, Nucl. Technol. 68 (1985) 18-28, https://doi.org/10.13182/NT85-A33563.
[30] H. Shi, Alumina forming alloys (steels, high entropy materials) for the mitigation of compatibility issues with liquid metals and steam in energy related, high-temperature applications, Karlsruher Institut für Technologie (KIT), Karlsruhe, 2020, https://doi.org/10.5445/IR/1000105453.
[31] H. Shi, C. Tang, A. Jianu, R. Fetzer, A. Weisenburger, M. Steinbrueck, M. Grosse, R. Stieglitz, G. Müller, Oxidation behavior and microstructure evolution of alumina-forming austenitic & high entropy alloys in steam environment at 1200 °C, Corros. Sci. (2020) 108654, https://doi.org/10.1016/j.corsci.2020.108654.
[32] B. Gwalani, D. Choudhuri, V. Soni, Y. Ren, M. Styles, J.Y. Hwang, S.J. Nam, S.H. Hong, R. Banerjee, Cu assisted stabilization and nucleation of L12 precipitates in $Al_{0.3}CuFeCrNi_2$ fcc-based high entropy alloy, Acta Mater. 129 (2017) 170-182, https://doi.org/10.1016/j.actamat.2017.02.053.
[33] M. Wang, H. Cui, Y. Zhao, C. Wang, N. Wei, Y. Zhao, X. Zhang, Q. Song, A simple strategy for fabrication of an FCC-based complex concentrated alloy coating with hierarchical nanoprecipitates and enhanced mechanical properties, Mater. Des. 180 (2019) 107893, https://doi.org/10.1016/j.matdes.2019.107893.
[34] M. Wang, G. Zhang, H. Cui, Y. Lu, Y. Zhao, N. Wei, T. Li, Effect of plasma remelting on microstructure and properties of a $CoCrCuNiAl_{0.5}$ high-entropy alloy prepared by spark plasma sintering, J. Mater. Sci. 56 (2021) 5878-5898, https://doi.org/10.1007/s10853-020-05570-x.
[35] S.G. Ma, Y. Zhang, Effect of Nb addition on the microstructure and properties of AlCoCrFeNi high-entropy alloy, Mater. Sci. Eng. A. 532 (2012) 480-486, https://doi.org/10.1016/j.msea.2011.10.110.
[36] S. Wolff-Goodrich, A. Marshal, K.G. Pradeep, G. Dehm, J.M. Schneider, C. Liebscher, Combinatorial Exploration of B2/$L2_1$ Precipitation Strengthened AlCrFeNiTi Compositionally Complex Alloys, J. Alloys Compd. 853 (2019) 156111, https://doi.org/10.1016/j.jallcom.2020.156111.
[37] J. Dąbrowa, G. Cieślak, M. Stygar, K. Mroczka, K. Berent, T. Kulik, M. Danielewski, Influence of Cu content on high temperature oxidation behavior of $AlCoCrCu_xFeNi$ high entropy alloys (x= 0; 0.5; 1), Intermetallics 84 (2017) 52-61, https://doi.org/10.1016/j.intermet.2016.12.015.
[38] H.M. Daoud, A.M. Manzoni, R. Völkl, N. Wanderka, U. Glatzel, Oxidation Behavior of $Al_8Co_{17}Cr_{17}Cu_8Fe_{17}Ni_{33}$, $Al_{23}Co_{15}Cr_{23}Cu_8Fe_{15}Ni_{15}$, and $Al_{17}Co_{17}Cr_{17}Cu_{17}Fe_{17}Ni_{17}$ Compositionally Complex Alloys (High-Entropy Alloys) at Elevated Temperatures in Air, Adv. Eng. Mater. 17 (2015) 1134-1141, https://doi.org/10.1002/adem.201500179.

[39] Y.Y. Liu, Z. Chen, Y.Z. Chen, J.C. Shi, Z.Y. Wang, S. Wang, F. Liu, Effect of Al content on high temperature oxidation resistance of Al_xCoCrCuFeNi high entropy alloys (x= 0, 0.5, 1, 1.5, 2), Vacuum 169 (2019) 108837, https://doi.org/10.1016/j.vacuum.2019.108837.
[40] S. Hayashi, D. Kudo, R. Nagashima, H. Utsumi, Effect of Cu on oxidation behaviour of FCC Fe-Ni-Cr-Al and Ni-Cr-Al based alloys, Corros. Sci. 163 (2020) 108273, https://doi.org/10.1016/j.corsci.2019.108273.
[41] T.T. Shun, C.H. Hung, C.F. Lee, The effects of secondary elemental Mo or Ti addition in $Al_{0.3}$CoCrFeNi high-entropy alloy on age hardening at 700 °C, J. Alloys Compd. 495 (2010) 55-58, https://doi.org/10.1016/j.jallcom.2010.02.032.
[42] Y. Wang, S. Ma, X. Chen, J. Shi, Y. Zhang, J. Qiao, Optimizing mechanical properties of AlCoCrFeNiTi_x high-entropy alloys by tailoring microstructures, Acta. Metall. Sin. (English Letters), 26 (2013) 277-284, https://doi.org/10.1007/s40195-012-0174-5.
[43] M.H. Chuang, M.H. Tsai, W.R. Wang, S.J. Lin, J.W. Yeh, Microstructure and wear behavior of $Al_xCo_{1.5}CrFeNi_{1.5}Ti_y$ high-entropy alloys, Acta Mater. 59 (2011) 6308-6317, ttps://doi.org/10.1016/j.actamat.2011.06.041.
[44] Y.J. Chang, A.C. Yeh, The evolution of microstructures and high temperature properties of $Al_xCo_{1.5}CrFeNi_{1.5}$Tiy high entropy alloys, J. Alloys Compd. 653 (2015) 379-385, https://doi.org/10.1016/j.jallcom.2015.09.042.
[45] J.Y. He, H. Wang, H.L. Huang, X.D. Xu, M.W. Chen, Y. Wu, X.J. Liu, T.G. Nieh, K. An, Z.P. Lu, A precipitation-hardened high-entropy alloy with outstanding tensile properties, Acta Mater. 102 (2016) 187-196, https://doi.org/10.1016/j.actamat.2015.08.076.
[46] A. Erdogan, K.M. Doleker, S. Zeytin, Effect of Al and Ti on High-Temperature Oxidation Behavior of CoCrFeNi-Based High-Entropy Alloys, JOM 71 (2019) 3499-3510, https://doi.org/10.1007/s11837-019-03679-2.
[47] L. Huang, X.J. Wang, B.X. Huang, C.Z. Wang, Study on Microstructure and Corrosion Resistance of AlCoCrFeNiTi(x) High-Entropy Alloys, MS&E 774 (2020) 012058, doi:10.1088/1757-899X/774/1/012058.
[48] Y. Yu, P. Shi, K. Feng, J. Liu, J. Cheng, Z. Qiao, J. Yang, J.S. Li, W. Liu, Effects of Ti and Cu on the Microstructure Evolution of AlCoCrFeNi High-Entropy Alloy During Heat Treatment, Acta. Metall. Sin. (English Letters) (2020) 1-14, https://doi.org/10.1007/s40195-020-01002-6.
[49] M.J. Rawlings, C.H. Liebscher, M. Asta, D.C. Dunand, Effect of titanium additions upon microstructure and properties of precipitation-strengthened Fe-Ni-Al-Cr ferritic alloys, Acta Mater. 128 (2017) 103-112, https://doi.org/10.1016/j.actamat.2017.02.028.
[50] Z.S. Nong, J.C. Zhu, R.D. Zhao, Prediction of structure and elastic properties of AlCrFeNiTi system high entropy alloys, Intermetallics 86 (2017) 134-146, https://doi.org/10.1016/j.intermet.2017.03.014.
[51] D. Choudhuri, T. Alam, T. Borkar, B. Gwalani, A.S. Mantri, S.G. Srinivasan, M.A. Gibson, R. Banerjee, Formation of a Huesler-like $L2_1$ phase in a CoCrCuFeNiAlTi high-entropy alloy, Scr. Mater. 100 (2015) 36-39, https://doi.org/10.1016/j.scriptamat.2014.12.006.
[52] A.M. Manzoni, S. Singh, H.M. Daoud, R. Popp, R. Völkl, U. Glatzel, N. Wanderka, On the path to optimizing the Al-Co-Cr-Cu-Fe-Ni-Ti high entropy alloy family for high temperature applications, Entropy 18 (2016) 104, https://doi.org/10.3390/e18040104.
[53] S.G. Ma, Y. Zhang, Effect of Nb addition on the microstructure and properties of AlCoCrFeNi high-entropy alloy, Mater. Sci. Eng. A. 532 (2012) 480-486, https://doi.org/10.1016/j.msea.2011.10.110.
[54] Y. Zhang, X. Yang, P.K. Liaw, Alloy design and properties optimization of high-entropy alloys, JOM 64 (2012) 830-838, https://doi.org/10.1007/s11837-012-0366-5.
[55] W.H. Liu, J.Y. He, H.L. Huang, H. Wang, Z.P. Lu, C.T. Liu, Effects of Nb additions on the microstructure and mechanical property of CoCrFeNi high-entropy alloys, Intermetallics 60 (2015) 1-8, https://doi.org/10.1016/j.intermet.2015.01.004.

[56] A.Y. Churyumov, A.V. Pozdniakov, A.I. Bazlov, H. Mao, V.I. Polkin, D.V. Louzguine-Luzgin, Effect of Nb Addition on Microstructure and Thermal and Mechanical Properties of Fe-Co-Ni-Cu-Cr Multiprincipal-Element (High-Entropy) Alloys in As-Cast and Heat-Treated State, JOM 71 (2019) 3481-3489, https://doi.org/10.1007/s11837-019-03644-z.

[57] S. Antonov, M. Detrois, S. Tin, Design of novel precipitate-strengthened Al-Co-Cr-Fe-Nb-Ni high-entropy superalloys, Metall. Mater. Trans. A 49 (2018) 305-320, https://doi.org/10.1007/s11661-017-4399-9.

[58] M. Detrois, S. Antonov, S. Tin, Phase stability and thermodynamic database validation in a set of non-equiatomic Al-Co-Cr-Fe-Nb-Ni high-entropy alloys, Intermetallics 104 (2019) 103-112, https://doi.org/10.1016/j.intermet.2018.11.002.

[59] M. Zhang, L. Zhang, P.K. Liaw, G. Li, R. Liu, Effect of Nb content on thermal stability, mechanical and corrosion behaviors of hypoeutectic $CoCrFeNiNb_x$ high-entropy alloys, J. Mater. Res. 33 (2018) 3276-3286, DOI: 10.1557/jmr.2018.103.

[60] C. Schroer, Guidelines for Corrosion Testing in Liquid Metals (Pb, LBE), MATTER Project, deliverable report D3.4, (2011-2015), 26 (accessed 05/03/2021), http://www.eera-jpnm.eu/filesharer/documents/_Euratom_Projects/Past%20projects/MATTER%20public%20deliverables/Deliverable%20D3.4%20MATTER.pdf

[61] Y. Zhang, Y.J. Zhou, J.P. Lin, G.L. Chen, P.K. Liaw, Solid-solution phase formation rules for multi-component alloys, Adv. Eng. Mater. 10 (2008) 534-538, https://doi.org/10.1002/adem.200700240.

[62] S. Guo, C. Ng, J. Lu, C.T. Liu, Effect of valence electron concentration on stability of fcc or bcc phase in high entropy alloys, J. Appl. Phys. 109 (2011) 103505, https://doi.org/10.1063/1.3587228.

[63] M.H. Chuang, M.H. Tsai, W.R. Wang, S.J. Lin, J.W. Yeh, Microstructure and wear behavior of $Al_xCo_{1.5}CrFeNi_{1.5}Ti_y$ high-entropy alloys, Acta Mater. 59 (2011) 6308-6317, https://doi.org/10.1016/j.actamat.2011.06.041.

[64] S. Mahadevan, S. Nalawade, J.B. Singh, A. Verma, B. Paul, K. Ramaswamy, Evolution of δ phase microstructure in alloy 718, In Proceedings of the 7th International Symposium on Superalloy, 718 (2010) 737-750, ISBN: 9781617827709.

[65] Z. Moser, W. Gąsior, K. Rzyman, A. Dębski, Calorimetric studies of the enthalpies of formation of $NiTi_2$, NiTi and Ni_3Ti, Arch. Metall. Mater. 51 (2006) 606-608,

[66] R. Hu, P. Nash, Experimental enthalpies of formation of compounds in Al-Ni-X systems, J. Mater. Sci. 41 (2006) 631-641, https://doi.org/10.1007/s10853-006-6479-x.

[67] T.M. Butler, M.L. Weaver, Oxidation behavior of arc melted AlCoCrFeNi multi-component high-entropy alloys, J. Alloys Compd. 674 (2016) 229-244, https://doi.org/10.1016/j.jallcom.2016.02.257.

[68] L.J. Santodonato, Y. Zhang, M. Feygenson, C.M. Parish, M.C. Gao, R.J. Weber, J.C. Neuefeind, Z. Tang, P.K. Liaw, Deviation from high-entropy configurations in the atomic distributions of a multi-principal-element alloy, Nat. Commun. 6 (2015) 1-13, https://doi.org/10.1038/ncomms6964.

[69] J.M. Zhu, J.L. Meng, J.L. Liang, Microstructure and mechanical properties of multi-principal component $AlCoCrFeNiCu_x$ alloy, Rare Metals, 35 (2016) 385-389, DOI 10.1007/s12598-014-0268-5.

[70] X.W. Qiu, C.X. Huang, M.J. Wu, C.G. Liu, Y.P. Zhang, Structure and properties of AlCrFeNiCuTi six principal elements equimolar alloy, J. Alloys Compd. 658 (2016) 1-5, https://doi.org/10.1016/j.jallcom.2015.10.224.

[71] K.L. Luthra, Stability of protective oxide films on Ti-base alloys, Oxid. Met. 36 (1991) 475–490, https://doi.org/10.1007/BF01151593.

[72] A. Weisenburger, A. Jianu, S. Doyle, M. Bruns, R. Fetzer, A. Heinzel, M. DelGiacco, W. An, G. Müller, Oxide scales formed on Fe–Cr–Al-based model alloys exposed to oxygen containing molten lead, J. Nucl. Mater. 437 (2013) 282–292, https://doi.org/10.1016/j.jnucmat.2013.02.044.

[73] G. Lütjering, J. C. Williams, Titanium, Springer, Berlin, 2003, p. 48, https://doi.org/10.1007/978-3-540-73036-1_2.
[74] A. Donchev, M. Schütze, Minimization of the Oxygen Embrittlement of Ti-Alloys, Theodor-Heuss-Allee, 25 60486, https://dechema-dfi.de/kwi_media/Downloads/ochtemperaturwerkstoffe/Projekte/high_temperature_materials_poster_tial_o_embrittlement1.pdf.
[75] J.M. Macak, C. Zollfrank, B.J. Rodriguez, H. Tsuchiya, M. Alexe, P. Greil, P. Schmuki, Ordered ferroelectric lead titanate nanocellular structure by conversion of anodic TiO_2 nanotubes, Adv. Mater. 21 (2009) 3121-3125, https://doi.org/10.1002/adma.200900587.
[76] M.P. Brady, Y. Yamamoto, M.L. Santella, L.R. Walker, Composition, microstructure, and water vapor effects on internal/external oxidation of alumina-forming austenitic stainless steels, Oxid. Met. 72 (2009) 311. https://doi.org/10.1007/s11085-009-9161-2.
[77] M.A. Mota, A.A. Coelho, J.M.Z. Bejarano, S. Gama, R. Caram, Fe–Al–Nb phase diagram investigation and directional growth of the $(Fe,Al)_2Nb$–$(Fe,Al,Nb)_{ss}$ eutectic system, J. Alloys Compd. 399 (2005) 196-201, https://doi.org/10.1016/j.jallcom.2005.03.038.
[78] C.C. Tung, J.W. Yeh, T.T. Shun, S.K. Chen, Y.S. Huang, H.C. Chen, On the elemental effect of AlCoCrCuFeNi high-entropy alloy system, Mater. Lett. 61 (2007) 1-5, https://doi.org/10.1016/j.matlet.2006.03.140.
[79] A. Takeuchi, A. Inoue, Classification of bulk metallic glasses by atomic size difference, heat of mixing and period of constituent elements and its application to characterization of the main alloying element, Mater. Trans 46 (2005) 2817-2829, https://doi.org/10.2320/matertrans.46.2817.
[80] R. Yang, J.A. Leake, R.W. Cahn, A microstructural study of a Ni_2AlTi–$Ni(Al,Ti)$–$Ni_3(Al,Ti)$ three-phase alloy, J. Mater. Res. 6 (1991) 343-354, https://doi.org/10.1557/JMR.1991.0343.
[81] Y.J. Chang, A.C. Yeh, The evolution of microstructures and high temperature properties of $Al_xCo_{1.5}CrFeNi_{1.5}Ti_y$ high entropy alloys, J. Alloys Compd. 653 (2015) 379-385, https://doi.org/10.1016/j.jallcom.2015.09.042.
[82] Y. Yamamoto, M.P. Brady, Z.P. Lu, C.T. Liu, M. Takeyama, P.J. Maziasz, B.A. Pint, Alumina-forming austenitic stainless steels strengthened by laves phase and MC carbide precipitates, Metall. Mater. Trans. A. 38 (2007) 2737-2746, https://doi.org/10.1007/s11661-010-0295-2.